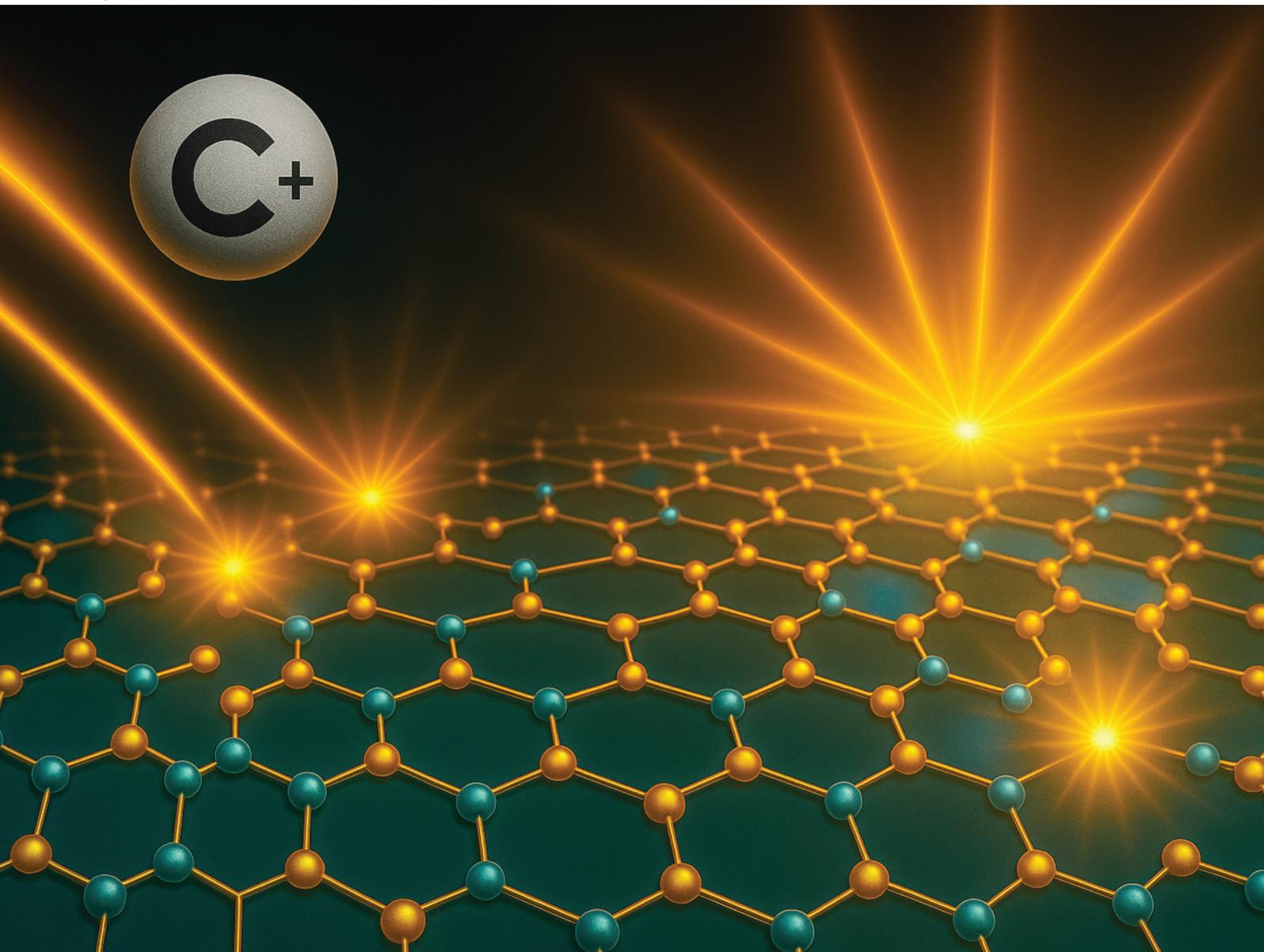# Nanoscale

PAPER
Thomas E. Gage, Jian-Min Zuo, Benjamin T. Diroll,
Jianguo Wen *et al.*
Deterministic fabrication of highly reproducible
monochromatic quantum emitters in hexagonal boron
nitride

NCNST

PAPER

Deterministic fabrication of highly reproducible monochromatic quantum emitters in hexagonal boron nitride

Muchuan Hua, [ID] [a] Wei-Ying Chen,[b] Hanyu Hou,[a,c]
Venkata Surya Chaitanya Kolluru, [ID] [a] Maria K. Y. Chan, [ID] [a] Haihua Liu,[a]
Thomas E. Gage,*[a] Jian-Min Zuo, [ID] *[c] Benjamin T. Diroll [ID] *[a] and
Jianguo Wen [ID] *[a]

Quantum emitters in hexagonal boron nitride are important room temperature single-photon sources. However, conventional fabrication methods yield quantum emitters with dispersed and inconsistent spectral profiles, limiting their potential for practical quantum applications, which demand reproducible high quality single-photon sources. Here, we report the deterministic creation of highly reproducible monochromatic quantum emitters by applying carbon-ion implantation on freestanding hexagonal boron nitride flakes, while a carbon mask with suitable thickness was adapted to optimize the implantation results. Quantum emitters fabricated using this approach exhibited thermally limited monochromaticity, with an emission center wavelength of 590.7 ± 2.7 nm, a narrow full width at half maximum of 7.1 ± 1.7 nm, an emission rate of 1 MHz without optical engineering, and exceptional stability under ambient conditions. Density functional theory calculations and scanning transmission electron microscopy suggest that these emitters are comprised of boron centered carbon tetramers. This method provides a reliable single-photon source for optical quantum computing and potential future industry-scale applications.

Introduction

Quantum information science (QIS) is an emerging field at the intersection of quantum physics, computer science, and information theory. It uses the basic rules of quantum mechanics to handle and process information in ways that traditional computing cannot match. Various materials and devices are being actively investigated as platform technologies for QIS,[1–7] with photon-based quantum information processing, communication, and transduction emerging as key areas within the field. These photon-based systems have distinct advantages, including long-lived quantum states, minimal environmental interference, and the capability to transmit quantum information over long distances through optical fibers.[8–11] The essential component of these systems is a quantum emitter (QE) that can stably produce indistinguishable single photons

at a high emission rate, and many efforts have been made towards QE fabrication upon different materials and platforms.[12–15]

Two-dimensional (2D) materials, such as transition metal dichalcogenides and hexagonal boron nitride (hBN), have been found to be possible hosts for QEs, attracting significant research interest in the last decade.[16–22] In particular, hBN has been extensively studied for QE creation as its large electronic band gap and optical phonon energy, in principle, allow it to host QEs at room temperature with perfect monochromaticity.[23–28] Existing approaches have successfully achieved spatial control in the creation of QEs; however, most of them have limited control of QEs' spectral properties (random emission wavelength with a broad intensity profile), limiting their practical use. Recently, both theoretical and experimental studies have suggested that carbon related defects are major sources of visible (from 435 nm to 700 nm) QEs in hBN.[20,29–37] Thus, an improved carbon implantation method for hBN with controlled defect creation is valuable not only for improving the generated QEs' repeatability and quality, but also for significantly reducing the complexity in identifying correlations between defect atomic structures and the observed single-photon emission behaviors.

[a]Center for Nanoscale Materials, Argonne National Laboratory, 9700 S. Cass Avenue, Lemont, 60439 Illinois, USA. E-mail: jwen@anl.gov
[b]Nuclear Science and Engineering, Argonne National Laboratory, 9700 S. Cass Avenue, Lemont, 60439 Illinois, USA
[c]Materials Science & Engineering, University of Illinois Urbana Champaign, 1304 W. Green St. MC 246, Urbana, 61801 Illinois, USA

In this study, we report a deterministic QE creation for freestanding hBN flakes through masked-carbon-ion-implantation (MCI), yielding two types of room temperature QEs with reproducible atom-like emission profiles. The QEs created using this process have remarkable monochromaticity with a standard deviation of 2.5 nm in zero phonon line (ZPL) wavelengths and a typical full-width-at-half-maximum (FWHM) under 25 meV at room temperature. In addition to single-photon behaviors, they are also exceptionally stable (no observable degradation after days with 10^5 W cm^{-2} laser excitation) and bright (1 MHz emission rate). With the help of first-principles density functional theory defect calculations and scanning transmission electron microscopy, the QEs were determined as radical carbon tetramers centered at boron sites.
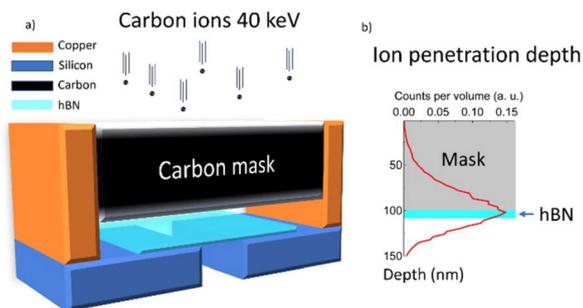

Fig. 1 (a) Scheme of the masked-carbon-ion implantation process. (b) Simulated penetration depth of the carbon ions (the curve was obtained with a 100 nm carbon mask and a 5 nm thick hBN flake).

Results and discussion

To achieve more consistent creation of carbonaceous defects in hBN with desired optical properties, typical ion bombardment procedures were modified to minimize lattice damage and generate defects in the middle of an hBN flake. This was achieved by employing an amorphous carbon mask, placed in front of the freestanding hBN flake to decelerate incoming carbon ions (Fig. 1a). The masks were designed and fabricated with a thickness that ensures that the carbon ions' most probable penetration depth aligns with the middle of the hBN flake; for example, a 100 nm thick carbon mask was used for a 16 monolayer hBN flake (Fig. 1b) to achieve the maximum stopping efficiency of carbon ions.[38] Such a configuration maximized the doping efficiency, with less damage due to other defects such as vacancies (details are given in the SI). Meanwhile, typical contamination caused by the recoiling of the mask elements was automatically precluded as the mask and the implantation ions were made of the same element. The authors note that reducing the ion acceleration energy could also lead to shallower implantation depths, potentially eliminating the need for a carbon mask. However, the IVEM-Tandem facility used in this study currently supports a minimum energy of 40 kV. To minimize the intrinsic defects of the sample, for instance the defects created during the synthesis, hBN flakes exfoliated from high-quality pristine crystal bulk were used. Since previous work on the optical properties of the QEs created by carbon-ion-implantation has found strong substrate dependence,[31] in this research, the hBN flakes were stamped onto Si or SiN transmission electron microscopy (TEM) grids with pre-fabricated apertures by the dry-transfer method[39] to eliminate the influence of the substrate. As shown in Fig. 2a, successful sample
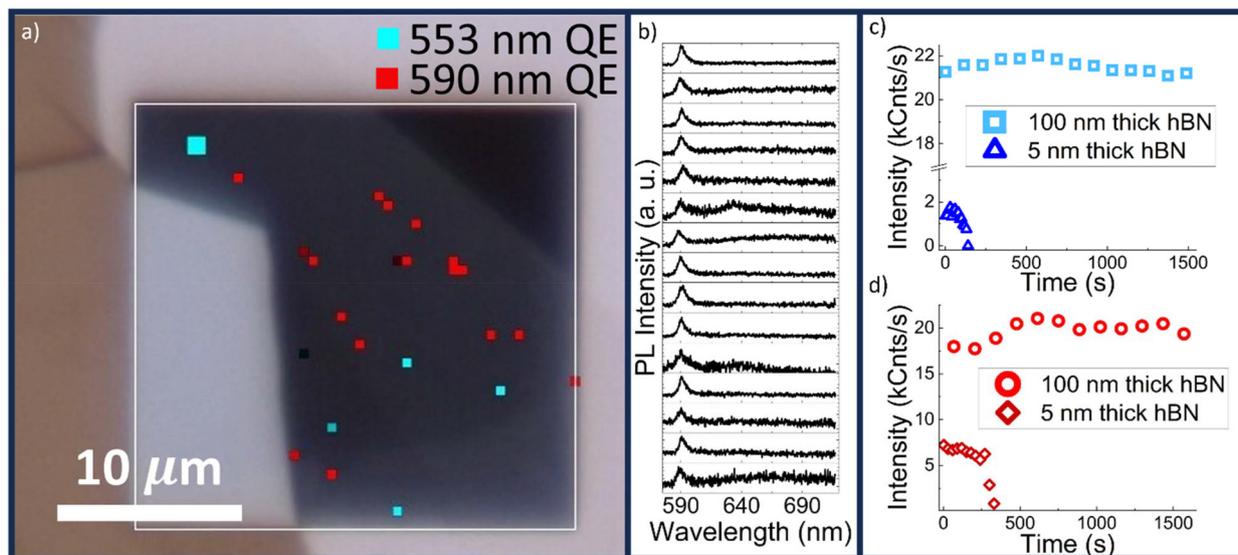
Fig. 2 (a) PL hypermapping of a typical hBN sample. (b) PL spectra of the 590 nm QEs (marked in red) in the map. (c) Typical PL intensity *versus* time of the 553 nm QEs generated in 5 nm (blue triangles) and 100 nm (light blue squares) thick hBN samples. (d) Typical PL intensity *versus* time of the 590 nm QEs generated in 5 nm (maroon diamonds) and 100 nm (red circles) thick hBN samples.

preparation resulted in an hBN flake with a freestanding area larger than 100 μm².

During a typical carbon-ion implantation process, a fluence of 2.5×10^6 ions per μm² with a 40 keV acceleration energy was applied to achieve a moderate emitter density (around 0.03 cts per μm² for a sample thickness of <10 nm).

Without applying any post treatment, such as high temperature annealing, preliminary scanning of the samples' PL signal was carried out using a reflective confocal microscope system (details are given in the Methods section in SI). A full photoluminescence (PL) spectrum was obtained at each scanning point, from which the intensities at 553 nm and 590 nm were extracted to generate spatial maps that were then overlaid on the optical image to show emitter distribution. Fig. 2a shows the overlaid map, also called PL intensity hyper-mapping, of a typical hBN flake treated with MCI, revealing localized QEs under 532 nm laser excitation. Most observed QEs can be categorized into two types: one with an emission wavelength peaking around 553 nm (coloured in cyan in Fig. 2a) and the other with an emission wavelength peaking around 590 nm (coloured in red in Fig. 2a). In the rest of the paper, these will be denoted as 553 nm and 590 nm QEs, respectively. The 553 nm QEs were consistent with those reported in a recent paper by Zhong *et al.*, obtained through carbon ion implantation followed by annealing treatment.[37] The spectra of the 590 nm QEs presented in Fig. 2a are plotted in Fig. 2b, demonstrating extraordinary consistency in their spectral profiles.

However, the QEs created in samples with thickness less than 10 nm were generally unstable, with their emission lasting only hundreds of seconds under continuous illumination under ambient conditions. As illustrated in the plots of PL intensity *versus* illumination time for the 553 nm and 590 nm QEs created in a 5 nm thick hBN sample, as shown in Fig. 2c (blue triangles) and Fig. 2d (maroon diamonds), respectively, the emission rates diminished after 120 s and 300 s, respectively. Given the small phonon side band (PSB) observed in these QEs, it is reasonable to infer that the defects are mechanically well isolated, with rigid defect structures and an intact surrounding lattice. Meanwhile, some emitters disappeared after months of storage in air. This is consistent with previous literature, which has identified reactions of oxygen with carbonaceous defects in hBN as the source of optical instability in thin flakes (such as 16 monolayers) of hBN.[34] The thin samples result in implantation of defects close to the hBN surface and can result in over penetration, which may leave pores for gas transport. Therefore, the authors concluded that exposing QEs to the environment led to their instability. Since the carbon mask is a separate, free-standing amorphous carbon film used solely to decelerate incoming ions during implantation, it does not play a role in passivating surface defects or mitigating oxygen diffusion as it is not directly coated onto the hBN flakes.

To solve the stability issue, a 50 nm carbon mask over a 100 nm hBN flake sample was selected to achieve a 91.7% stopping efficiency of the carbon ions with negligible over

penetration (details are given in the SI). After applying MCI to the sample, QEs were created with a total QE areal density of 0.42 cts per μm², an order of magnitude higher than that for the thin samples with identical ion irradiation fluence. The spectral line profiles of the emitters found in the thick films match those of the thin films, but with significantly enhanced stability. Typical PL intensity *versus* time plots for the 553 nm and 590 nm QEs are shown in Fig. 2c (light blue squares) and d (red circles) respectively. No brightness degradation was observed for prolonged illumination with long term fluctuations attributed to the drifting of the stage. The population distributions at wavelengths of the QEs created in the thin and thick samples are almost identical, where 553.5 ± 2.7 nm and 590.7 ± 2.5 nm (Fig. 3g) were obtained from the combined data. Due to fixed acceleration voltage in our current setup, the effect of implantation energy on ZPL distribution was not explored. However, we investigated the influence of fluence and found no notable change in ZPL distribution within the tested fluence range. This may be attributed to the low implanted ion density, where the average spacing between emitters remains larger than their interaction range. Besides the 553 nm and 590 nm QEs, other emitters were much less
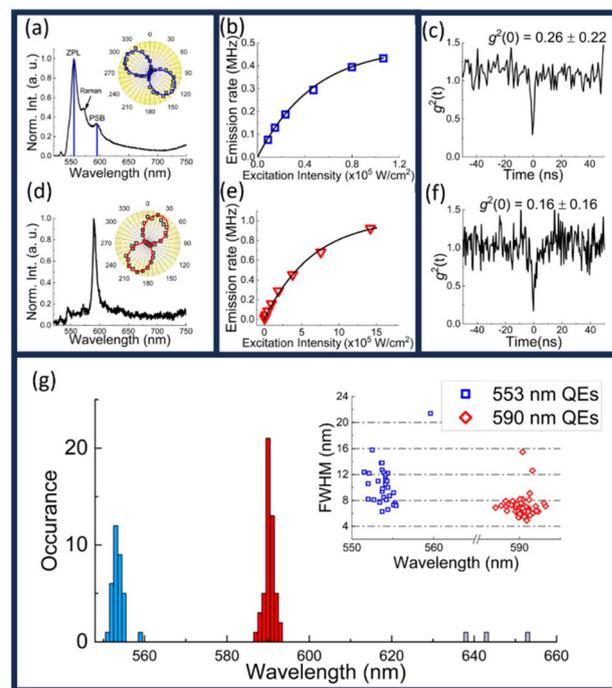

Fig. 3 Optical characterization of the QEs. (a) PL spectrum of a typical 553 nm QE, inset: PL intensity as a function of the linear polarization angle of the excitation laser beam. (b) PL intensity as a function of the excitation power for a typical 553 nm QE (c) Photon second-order-correlation function of a typical 553 nm QE. (d) PL spectrum of a typical 590 nm QE, inset: PL intensity as a function of the linear polarization angle of the excitation laser beam. (e) PL intensity as a function of the excitation power for a typical 590 nm QE. (f) Photon second order correlation function of a typical 590 nm QE. (g) Emitters' ZPL wavelength distribution with a bar width of 1 nm. The inset shows the FWHM of the 553 nm (hollow blue triangles) and 590 nm (hollow red diamonds) QEs.

likely (3.4% among the created emitters) to be found in our samples, suggesting that the defect creation was dominated by two ultimate processes. As shown in Fig. 3d, the typical spectrum of a 553 nm QE was slightly cut on the short wavelength side as multiple 547 nm long pass filters were used to completely remove the excitation laser light (532 nm CW laser). The sharp feature was still pronounced enough for us to estimate the FWHM to be 10.5 ± 3 nm (43 meV, blue triangles in the inset in Fig. 3g). Besides the Raman signal of hBN, a secondary peak around 596 nm, 161 meV from the ZPL, which is slightly lower than the optical phonon energy of hBN, about 170 meV,[40,41] was observed and has been attributed to the PSB. In contrast, the 590 nm QEs not only showed a much narrower emission profile but also a smaller dispersion of the FWHM, with a value of 7.1 ± 1.7 nm (25 meV, red diamonds in the inset in Fig. 3g). A PSB at 636 nm (151 meV from the ZPL) was not pronounced except at high excitation laser power. The measured emission linewidths (FWHM) are 25 meV at room temperature ($k_B T \approx 25.2$ meV) and 7 meV at 87 K ($k_B T \approx 7.5$ meV), suggesting that the linewidth is predominantly limited by thermal broadening.

Saturation behaviours were observed in both types of QEs with increasing excitation laser power and the observed maximum emission rates of the 553 nm and 590 nm QEs were 0.43 MHz (Fig. 3b) and 0.92 MHz (Fig. 3e), respectively (considered as lower limits, details are given in the Methods section). Although the maximum emission rate of the 553 nm QEs is much lower than that of the 590 nm QEs, they saturate at lower excitation intensity (more than an order of magnitude smaller), suggesting that the 533 nm QEs have a larger absorption cross-section. This is also confirmed by the stability data, where PL intensity's long-term fluctuation for the 590 nm QEs was more pronounced as their collection efficiency is more sensitive to the drifting stage due to the small spatial dimension responsible for absorption (confirmed below using CL).

The excitation polarization dependence information of the QEs was obtained by rotating the laser's polarization angle, θ, with a half-wave-plate. The data are shown in the inset in Fig. 3g for 553 nm and 590 nm QEs, respectively, where the QEs' integrated PL emission intensity $I(\theta)$ can be fitted with the function,

$$I(\theta) = I_0 + I_A \times \sin^2(\theta - \theta_0), \quad (1)$$

by assuming the linear dipole response for the defects. Here the purity of the dipoles, p, was defined as, $p = I_A/(I_A + I_0)$ with a maximum value of 1, where I_0 and I_A denote the base value and the amplitude of the fitting function. According to our data, the p value approaching 1 was observed in both types of

QEs (typical values of 0.962 and 0.971 were observed in 553 nm and 590 nm QEs). Such an observation indicated that a single in-plane transition dipole moment was formed between the defects' ground and excited states.

Using a Hanbury–Brown–Twiss (HBT) interferometer, the anti-bunching behaviour originating from the single-photon nature of the defects' emission was confirmed (elaborated in the Methods section). As shown in Fig. 3c and f, $g^2(0)$ values of 0.26 ± 0.22 and 0.16 ± 0.16 were obtained for 553 nm and 590 nm QEs respectively, confirming their single-photon emission behaviour with high single-photon purity. According to the data, no profound photon bunching at time $\neq 0$ was observed in both types, suggesting the absence of non-radiative shelving state in their electronic states.[42] Therefore the QEs' anti-bunching data were fitted using a background corrected two-level system model[43]

$$g^2(t) = 1 - \eta^2 e^{-|t|/\tau} \quad (2)$$

$\eta = I_e/(I_e + I_b)$, where I_e and I_b denote the integrated emission intensity and background intensity, respectively. τ is the defect state's radiative decay mean cycle lifetime, which is the sum of the radiative excitation and decay lifetimes (statistics of the time-resolved data were obtained by fitting the data with eqn (2)). As shown in Table 1, a short radiative cycle lifetime was observed for both 553 nm (1.06 ± 0.48 ns) and 590 nm (0.69 ± 0.17 ns) QEs.

The freestanding sample also allows the characterization of the samples using a scanning transmission electron microscope-cathodoluminescence (STEM-CL) system, where the focused electron beam (e-beam) activates the defect-related emission. Fig. 4 shows the CL intensity mapping data collected from a 100 nm thick sample. The CL spectra were obtained by averaging over the bright pixels within the circled areas. According to the data, the CL spectra of the QEs showed identical wavelength and FWHM to their PL versions. Meanwhile, a much higher spatial resolution than the PL data was achieved, where locations of the 553 nm and 590 nm QEs were determined within 50 nm (Fig. 4a) and 4 nm (Fig. 4b), respectively. The radius of the excitation volume introduced by the e-beam, R_e, can be estimated using the empirical equation: $R_e = 1/\rho \times (0.0276M \times Z^{0.889}) \times E_b^{1.67}$ in units of μm,[44] where M is the molar mass (24.8 g mol^{-1}), ρ is the density (2.1 g cm^{-3}) and Z is the atomic number (the mean value of N and B, 6, was applied) of the target material. E_b denotes the energy of the e-beam in keV. For 80 keV acceleration energy, which is used in our experiment, $R_e = 99.5$ μm was estimated, which is much bigger than the thickness of the hBN flakes used in our experiment. Therefore, the excitation volume was roughly defined by

Table 1 Photoluminescence information of the quantum emitters. The values were obtained at room temperature in atmosphere

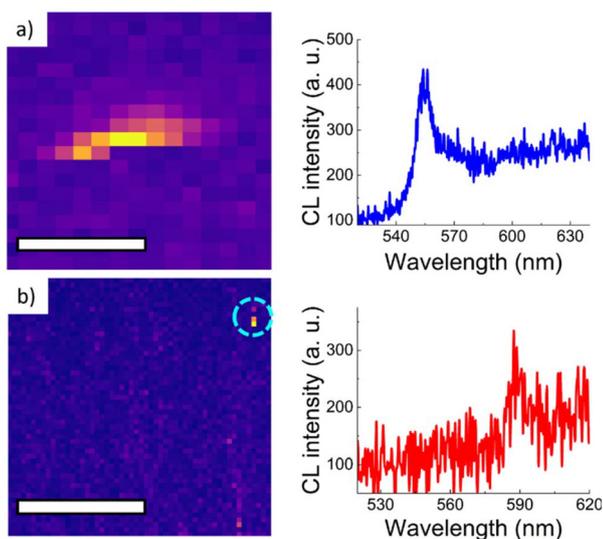| QE	τ_r	η	Peak wavelength	FWHM	Dipole
553 nm	1.06 ± 0.48 ns	0.860 ± 0.139	553.5 ± 2.7 nm	10.5 ± 3.0 nm	Yes
590 nm	0.69 ± 0.17 ns	0.915 ± 0.078	590.1 ± 2.5 nm	7.1 ± 1.7 nm	Yes

Fig. 4 STEM-CL intensity mapping of an MCI-treated 100 nm thick hBN flake. (a) Typical mapping of integrated CL intensity (from 547 nm to 563 nm) in the presence of a 553 nm QE (the spectrum was derived by averaging the bright pixels) and its spectrum is shown on the right. (b) Typical mapping of integrated CL intensity (from 584 nm to 596 nm) in the presence of a 590 nm QE (circled with cyan dash lines) and its spectrum.

the size of the e-beam,[45] which was much smaller than the size of the observed emission area. So, it is reasonable to consider that the interactive volume of the 590 nm QEs to electron beams was more than an order of magnitude smaller than that of the 553 nm QEs. This is consistent with the PL measurement, in which the photon absorption cross-section of the 590 nm QEs is smaller than that of the 553 nm QEs by a factor of 14, suggesting that the 590 nm QEs are spatially smaller than the 553 nm QEs. Therefore, a possible explanation is that a 553 nm QE's physical size is roughly an order of magnitude bigger than that of a 590 nm QE. As what will be discussed later in the paper, the likelihood of forming multi-carbon defects decreases exponentially as the number of carbon replacement sites increases. It is very unlikely for the 553 nm QEs to be giant carbon multimers. A reasonable guess would be that the origins of 553 nm QEs are clusters of carbon defects that are close to each other.[20,46] Recently, Faraon's group reported that carbon defect clusters forming a C_B–C_N donor–acceptor pair could potentially be the origins of the observed 553 nm QEs in hBN.[37] On the other hand, the 590 nm QEs are most likely attributed to single-defect mechanisms. This distinction can adequately explain the observed differences in the ZPL linewidth and PSB strength between the two types of QEs. Besides, the CL data also confirm the low emitter density observed in the PL experiment, as no clusters of the emitters were detected, and this further highlights the huge difference between the amount of carbon ions stopped by the flakes and the resulting emitter density. Here, we used the typical emitter density observed in a 100 nm thick hBN flake, 0.42 cts per μm^2, for analysis as it is stable. Compared to

the carbon ions stopped by the flake, 2.5×10^6 per μm^2, an intuitive speculation is that more than one carbon atom was required to form an emissive defect.

The subsequent analysis only focuses on the 590 nm QEs as they were more likely to have a single defect configuration. The identity of these single defects, however, is not immediately clear. By assuming that the stopping of the carbon ions is a completely stochastic process, and the aggregation of carbon ions were negligible, the surface density of n carbon ions replacing neighbouring lattice sites (forming carbon dimers, trimers or tetramers) within a monolayer of hBN, Γ_n, can be estimated by evaluating the possible configurations of carbon replacement. Since the concentration of carbon ions in each layer was estimated to be low ($<10^{-3}$), for each configuration, a lattice site being intact approaches 1. Therefore, Γ_n can be simply written in the form of (details are given in the SI):

$$\Gamma_n = \Gamma_s \cdot \sum_{i=1}^{N} \zeta_n \cdot (\Gamma_i \cdot V_{site})^{n-1}, \qquad (3)$$

where Γ_i denotes the concentration of carbon ions at the ith layer of the hBN flakes, which was obtained from the SRIM (the Stopping and Range of Ions in Matter) simulation. V_{site} denotes the average volume occupied by each lattice site. ζ_n denotes the number of possible configurations of n carbon ions replacing neighbouring sites. N is the total number of layers of the hBN flakes. Γ_s is the effective surface density measured at the implantation target. Γ_s and Γ_i satisfy the relationship: $\Gamma_s = \sum_{i=1}^{N} \Gamma_i = 2.5 \times 10^6$ per μm^2. According to eqn (3), the surface density of carbon dimers, trimers, and tetramers was estimated to be 627, 0.185, and 0.000967 per μm^2, respectively (details are given in the SI). Considering the possible aggregation of the carbon ions inside the hBN flakes and the self-repairing processes, the actual density was expected to be much higher than the estimated density, suggesting that, most likely, the emissive defects were carbon trimers or tetramers.

We utilized first-principles density functional theory (DFT) calculations to further validate the proposed defect structures (insets in Fig. 5a) that might be responsible for the observed emissions at 590 nm. We considered the carbon trimers C_{3B} (replacing NBN sites) and C_{3N} (replacing BNB sites) and radial tetramer defects C_{4B} (replacing BN_3 sites) and C_{4N} (replacing NB_3 sites) and performed DFT calculations with charged defects to predict the defect transition levels within the band gap. Here, we applied the charge defect calculations correction methodology in ref. 47 and calculated the charge defect formation energy E_f as a function of the Fermi energy, and the results for C_{4B}, C_{4N}, C_{3N}, and C_{3B} are shown in Fig. 5a (more details are given in the SI). The calculated electronic states based on the E_f analysis suggest that C_{4B} has a transition energy of 2.1 ± 0.2 eV corresponding to the +2/0 transition, which most closely agrees with the observed emission energy (2.10 eV). However, the calculated energy levels of C_{4N}, C_{3N}, and C_{3B} are approximately 2.9 eV, 3.6 eV, and 2.7 eV, respectively — significantly higher than the observed 2.1 eV and well
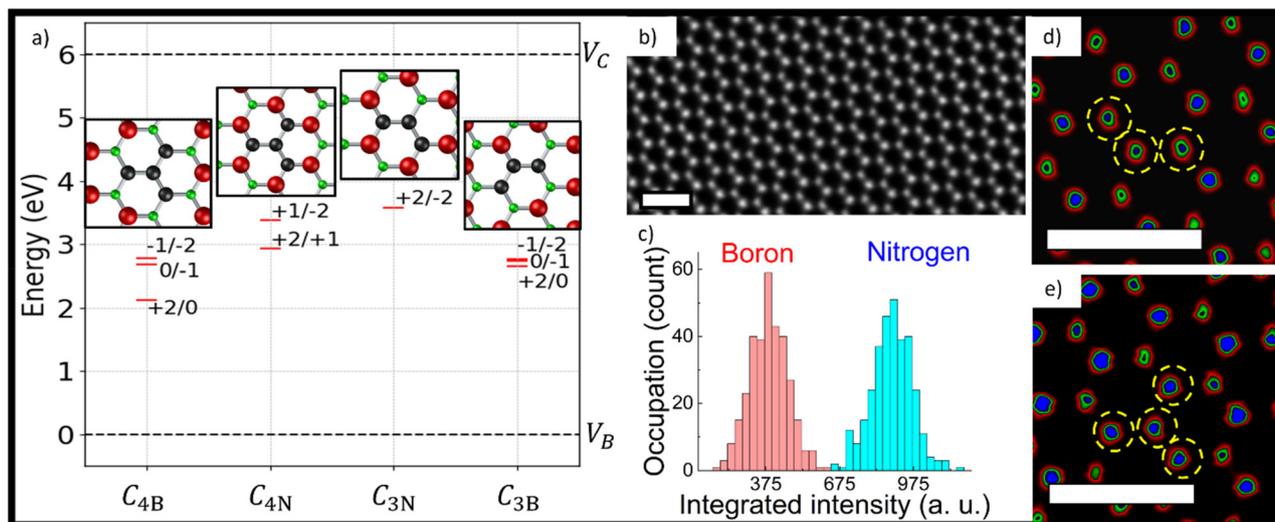
Fig. 5 DFT results and the atomic resolution STEM images of the MCI-treated hBN sample. (a) Allowed electronic energy states derived from DFT calculations for C_{4B}, C_{4N}, C_{3N} and C_{3B} (from left to right). The insets show the atomic model of the corresponding defects, where the green, black, and red spheres denote boron, carbon, and nitrogen atoms, respectively. (b) Typical ADF STEM image of the hBN flakes with less than 10 layers. (c) Histogram plot of the integrated intensity of each dot in (b). (d) False colour STEM image of carbon trimer defects C_{3N} replacing "BNB" sites. (e) False colour STEM image of carbon tetramers C_{4B} centred at the boron site. All scale bars denote 500 pm. Note: DFT calculations have an error margin of ±0.2 eV.

beyond the typical ±0.2 eV error margin of the applied DFT method (see the SI for details).

To corroborate the DFT prediction, atomic resolution STEM images of the samples were taken to reveal the atomic structures involved in the emission. A typical annular dark field (ADF) image of the MCI hBN sample with less than 10 layers taken over the emitter sites is shown in Fig. 5b, where the hexagonal structure of boron nitride was identified. The image was taken along the direction perpendicular to the flake plane. Here, the hBN crystals used in our experiment showed AA′ stacking, where boron and nitrogen sites were alternatively stacking on each other between layers. In such a configuration, two adjacent layers form columns of atoms with an identical total Z value, resulting in no contrast difference. Thus, for flakes with an even number of layers, the lattice sites exhibit identical intensity. In contrast, for flakes with an odd number of layers, the intensity difference between the boron and nitrogen sites of the non-compensated monolayer is retained. Therefore, the image in Fig. 5b was taken from an odd layer hBN flake, where the boron (dimmer) and nitrogen (brighter) sites can be well distinguished. As the number of layers increases, the contrast between B and N gradually decreases, but remains discernible for flakes thinner than 10 layers under the imaging conditions described in Methods. A statistical analysis is shown in Fig. 5c, where the histogram of the integrated intensity for each lattice site in Fig. 5b (the image shown is cropped to a quarter of the original one to match the scale) is plotted, showing unambiguous difference between the boron and nitrogen sites. Therefore, lattice sites with ADF image intensity in between the nitrogen and boron sites were attributed to carbon replacement ($Z = 6$). As shown in Fig. 5d

and e, carbon trimers replacing BNB sites and carbon tetramers replacing BN_3 sites (marked with yellow dashed circles) were observed, respectively. The data corroborate the formation of C_{4B} during the MCI process, consistent with the conclusion from the emitter density analysis and DFT calculations.

Conclusions

Masked-carbon-ion implantation (MCI) enables repeatable deterministic production of bright, stable and atom-like room temperature quantum emitters (QEs) in hBN, ensuring a highly consistent yield of QEs with excellent single photon purity. The mask approach is also inherently amenable for lithography, meaning that it has the ability to place QEs deterministically in space. Our research is of both technological and scientific interest, as it provides consistent reproducible QE sample production, enabling a reliable platform for characterization and fabrication research. According to our analysis, boron centred carbon tetramers, C_{4B}, were suggested to be the origins of the 590 nm QEs, while the 553 nm QEs are attributed to the donor–acceptor pairs induced by carbon-defect clusters. The QEs produced by this method exhibit exceptional stability, demonstrating the robustness of the approach. Such reliability is paramount when considering the demands of practical applications, especially industrial-scale production, where reproducibility and consistency are central to achieving standardized outputs. This work introduces a potentially transformative dimension to the landscape of quantum technology.

Author contributions

Conflicts of interest

There are no conflicts to declare.

Data availability

All data will be available at https://zenodo.org/records/15233137.

The SI contains the experimental methods, non-essential supporting data and arguments. Supplementary information is available. See DOI: https://doi.org/10.1039/d5nr01564b.

Acknowledgements

References

1 N. Y. Yao, L. Jiang, A. V. Gorshkov, P. C. Maurer, G. Giedke, J. I. Cirac and M. D. Lukin, *Nat. Commun.*, 2012, **3**, 800.

2 T. van der Sar, Z. H. Wang, M. S. Blok, H. Bernien, T. H. Taminiau, D. M. Toyli, D. A. Lidar, D. D. Awschalom, R. Hanson and V. V. Dobrovitski, *Nature*, 2012, **484**, 82–86.

3 H. Bernien, B. Hensen, W. Pfaff, G. Koolstra, M. S. Blok, L. Robledo, T. H. Taminiau, M. Markham, D. J. Twitchen, L. Childress and R. Hanson, *Nature*, 2013, **497**, 86–90.

4 G. Waldherr, Y. Wang, S. Zaiser, M. Jamali, T. Schulte-Herbrüggen, H. Abe, T. Ohshima, J. Isoya, J. F. Du, P. Neumann and J. Wrachtrup, *Nature*, 2014, **506**, 204–207.

5 B. Hensen, H. Bernien, A. E. Dréau, A. Reiserer, N. Kalb, M. S. Blok, J. Ruitenberg, R. F. L. Vermeulen, R. N. Schouten, C. Abellán, W. Amaya, V. Pruneri, M. W. Mitchell, M. Markham, D. J. Twitchen, D. Elkouss, S. Wehner, T. H. Taminiau and R. Hanson, *Nature*, 2015, **526**, 682–686.

6 C. E. Bradley, J. Randall, M. H. Abobeih, R. C. Berrevoets, M. J. Degen, M. A. Bakker, M. Markham, D. J. Twitchen and T. H. Taminiau, *Phys. Rev. X*, 2019, **9**, 031045.

7 X. Zhou, X. Li, Q. Chen, G. Koolstra, G. Yang, B. Dizdar, Y. Huang, C. S. Wang, X. Han, X. Zhang, D. I. Schuster and D. Jin, *Nat. Phys.*, 2024, **20**, 116–122.

8 S. Noda, A. Chutinan and M. Imada, *Nature*, 2000, **407**, 608–610.

9 R. Raussendorf, D. E. Browne and H. J. Briegel, *Phys. Rev. A*, 2003, **68**, 022312.

10 R. Raussendorf, S. Bravyi and J. Harrington, *Phys. Rev. A*, 2005, **71**, 062313.

11 N. Coste, D. A. Fioretto, N. Belabas, S. C. Wein, P. Hilaire, R. Frantzeskakis, M. Gundin, B. Goes, N. Somaschi, M. Morassi, A. Lemaître, I. Sagnes, A. Harouri, S. E. Economou, A. Auffeves, O. Krebs, L. Lanco and P. Senellart, *Nat. Photonics*, 2023, **17**, 582–587.

12 A. Lohrmann, N. Iwamoto, Z. Bodrog, S. Castelletto, T. Ohshima, T. J. Karle, A. Gali, S. Prawer, J. C. McCallum and B. C. Johnson, *Nat. Commun.*, 2015, **6**, 7783.

13 Y. Zhou, Z. Wang, A. Rasmita, S. Kim, A. Berhane, Z. Bodrog, G. Adamo, A. Gali, I. Aharonovich and W. Gao, *Sci. Adv.*, 2018, **4**, eaar3580.

14 J. Wang, Y. Zhou, Z. Wang, A. Rasmita, J. Yang, X. Li, H. J. von Bardeleben and W. Gao, *Nat. Commun.*, 2018, **9**, 4106.

15 W. Liu, V. Ivanov, K. Jhuria, Q. Ji, A. Persaud, W. Redjem, J. Simoni, Y. Zhiyenbayev, B. Kante, J. G. Lopez, L. Z. Tan and T. Schenkel, *Phys. Rev. Appl.*, 2023, **20**, 014058.

16 H. I. Rasool, C. Ophus and A. Zettl, *Adv. Mater.*, 2015, **27**, 5771–5777.

17 C. Chakraborty, L. Kinnischtzke, K. M. Goodfellow, R. Beams and A. N. Vamivakas, *Nat. Nanotechnol.*, 2015, **10**, 507–511.

18 G. Grosso, H. Moon, B. Lienhard, S. Ali, D. K. Efetov, M. M. Furchi, P. Jarillo-Herrero, M. J. Ford, I. Aharonovich and D. Englund, *Nat. Commun.*, 2017, **8**, 705.

19 S. Roy, X. Zhang, A. B. Puthirath, A. Meiyazhagan, S. Bhattacharyya, M. M. Rahman, G. Babu, S. Susarla, S. K. Saju, M. K. Tran, L. M. Sassi, M. A. S. R. Saadi, J. Lai, O. Sahin, S. M. Sajadi, B. Dharmarajan, D. Salpekar, N. Chakingal, A. Baburaj, X. Shuai, A. Adumbumkulath, K. A. Miller, J. M. Gayle, A. Ajnsztajn, T. Prasankumar, V. V. J. Harikrishnan, V. Ojha, H. Kannan, A. Z. Khater, Z. Zhu, S. A. Iyengar, P. A. da S. Autreto, E. F. Oliveira, G. Gao, A. G. Birdwell, M. R. Neupane, T. G. Ivanov, J. Taha-Tijerina, R. M. Yadav, S. Arepalli, R. Vajtai and P. M. Ajayan, *Adv. Mater.*, 2021, **33**, 2101589.

20 Q. Tan, J.-M. Lai, X.-L. Liu, D. Guo, Y. Xue, X. Dou, B.-Q. Sun, H.-X. Deng, P.-H. Tan, I. Aharonovich, W. Gao and J. Zhang, *Nano Lett.*, 2022, **22**, 1331–1337.

21 S. Li, G. Thiering, P. Udvarhelyi, V. Ivády and A. Gali, *Nat. Commun.*, 2022, **13**, 1210.

22 Z. Benedek, R. Babar, Á. Ganyecz, T. Szilvási, Ö. Legeza, G. Barcza and V. Ivády, *npj Comput. Mater.*, 2023, **9**, 187.

23 Y.-M. He, G. Clark, J. R. Schaibley, Y. He, M.-C. Chen, Y.-J. Wei, X. Ding, Q. Zhang, W. Yao, X. Xu, C.-Y. Lu and J.-W. Pan, *Nat. Nanotechnol.*, 2015, **10**, 497–502.

24 T. T. Tran, K. Bray, M. J. Ford, M. Toth and I. Aharonovich, *Nat. Nanotechnol.*, 2016, **11**, 37–41.

25 J. Ziegler, R. Klaiss, A. Blaikie, D. Miller, V. R. Horowitz and B. J. Alemán, *Nano Lett.*, 2019, **19**, 2121–2127.

26 X. Xu, Z. O. Martin, D. Sychev, A. S. Lagutchev, Y. P. Chen, T. Taniguchi, K. Watanabe, V. M. Shalaev and A. Boltasseva, *Nano Lett.*, 2021, **21**, 8182–8189.

27 A. B. D. Shaik and P. Palla, *Sci. Rep.*, 2021, **11**, 12285.

28 S. J. U. White, T. Yang, N. Dontschuk, C. Li, Z.-Q. Xu, M. Kianinia, A. Stacey, M. Toth and I. Aharonovich, *Light: Sci. Appl.*, 2022, **11**, 186.

29 S. A. Tawfik, S. Ali, M. Fronzi, M. Kianinia, T. T. Tran, C. Stampfl, I. Aharonovich, M. Toth and M. J. Ford, *Nanoscale*, 2017, **9**, 13575–13582.

30 B. Shevitski, S. M. Gilbert, C. T. Chen, C. Kastl, E. S. Barnard, E. Wong, D. F. Ogletree, K. Watanabe, T. Taniguchi, A. Zettl and S. Aloni, *Phys. Rev. B*, 2019, **100**, 155419.

31 N. Mendelson, D. Chugh, J. R. Reimers, T. S. Cheng, A. Gottscholl, H. Long, C. J. Mellor, A. Zettl, V. Dyakonov, P. H. Beton, S. V. Novikov, C. Jagadish, H. H. Tan, M. J. Ford, M. Toth, C. Bradac and I. Aharonovich, *Nat. Mater.*, 2016, **20**, 321–328.

32 N. R. Jungwirth and G. D. Fuchs, *Phys. Rev. Lett.*, 2017, **119**, 057401.

33 F. Hayee, L. Yu, J. L. Zhang, C. J. Ciccarino, M. Nguyen, A. F. Marshall, I. Aharonovich, J. Vučković, P. Narang, T. F. Heinz and J. A. Dionne, *Nat. Mater.*, 2020, **19**, 534–539.

34 K. Li, T. J. Smart and Y. Ping, *Phys. Rev. Mater.*, 2022, **6**, L042201.

35 Y. Chen, A. Gale, K. Yamamura, J. Horder, A. Condos, K. Watanabe, T. Taniguchi, M. Toth and I. Aharonovich, *Appl. Phys. Lett.*, 2023, **123**, 041902.

36 S. Sarkar, Y. Xu, S. Mathew, M. Lal, J.-Y. Chung, H. Y. Lee, K. Watanabe, T. Taniguchi, T. Venkatesan and S. Gradečak, *Nano Lett.*, 2024, **24**, 43–50.

37 D. Zhong, S. Gao, M. Saccone, J. R. Greer, M. Bernardi, S. Nadj-Perge and A. Faraon, *Nano Lett.*, 2024, **24**, 1106–1113.

38 J. F. Ziegler, M. D. Ziegler and J. P. Biersack, *Nucl. Instrum. Methods Phys. Res., Sect. B*, 2010, **268**, 1818–1823.

39 A. Castellanos-Gomez, M. Buscema, R. Molenaar, V. Singh, L. Janssen, H. S. J. van der Zant and G. A. Steele, *2D Mater.*, 2014, **1**, 011002.

40 S. Reich, A. C. Ferrari, R. Arenal, A. Loiseau, I. Bello and J. Robertson, *Phys. Rev. B:Condens. Matter Mater. Phys.*, 2005, **71**, 205201.

41 H. I. Røst, S. P. Cooil, A. C. Åsland, J. Hu, A. Ali, T. Taniguchi, K. Watanabe, B. D. Belle, B. Holst, J. T. Sadowski, F. Mazzola and J. W. Wells, *Nano Lett.*, 2023, **23**, 7539–7545.

42 P. Michler, A. Imamoğlu, M. D. Mason, P. J. Carson, G. F. Strouse and S. K. Buratto, *Nature*, 2000, **406**, 968–970.

43 R. Brouri, A. Beveratos, J.-P. Poizat and P. Grangier, *Opt. Lett.*, 2000, **25**, 1294–1296.

44 K. Kanaya and S. Okayama, *J. Phys. D:Appl. Phys*, 1972, **5**, 43–58.

45 B. G. Yacobi and D. B. Holt, *Cathodoluminescence Microscopy of Inorganic Solids*, Springer US, New York, 1990.

46 C. Freysoldt and J. Neugebauer, *Phys. Rev. B*, 2018, **97**, 205425.

47 G. Kresse and J. Furthmüller, *Comput. Mater. Sci.*, 1996, **6**, 15–50.